Available online at www.sciencedirect.com
ScienceDirect
Acta Materialia 59 (2011) 943–954
Acta MATERIALIA
www.elsevier.com/locate/actamat

Ambient- and high-temperature mechanical properties of isochronally aged Al–0.06Sc, Al–0.06Zr and Al–0.06Sc–0.06Zr (at.%) alloys

Keith E. Knipling [a,b,*], David N. Seidman [b,c], David C. Dunand [b]

[a] US Naval Research Laboratory, Multifunctional Materials Branch, Washington, DC 20375-0001, USA
[b] Department of Materials Science and Engineering, Northwestern University, Evanston, IL 60208-3108, USA
[c] Northwestern University Center for Atom-Probe Tomography (NUCAPT), Evanston, IL 60208-3108, USA

Received 7 May 2010; received in revised form 7 October 2010; accepted 8 October 2010
Available online 18 November 2010

Abstract

Ambient- and high-temperature precipitation strengthening are investigated in Al–0.06Sc, Al–0.06Zr and Al–0.06Sc–0.06Zr (at.%) alloys. Following solidification, Sc is concentrated at the dendrite peripheries while Zr is segregated at the dendrite cores. During isochronal aging, precipitation of Al_3Sc ($L1_2$) commences between 250 and 300 °C for Al–0.06Sc, and reaches a 429 MPa peak microhardness at 325 °C. For Al–0.06Zr, precipitation of Al_3Zr ($L1_2$) first occurs between 400 and 425 °C and reaches a 295 MPa peak microhardness at 475 °C. A pronounced synergistic effect is observed when both Sc and Zr are present. Above 325 °C, Zr additions provide a secondary strength increase that is attributed to precipitation of Zr-enriched outer shells onto the Al_3Sc precipitates, leading to a peak microhardness of 618 MPa at 400 °C for Al–0.06Sc–0.06Zr. Upon compressive creep deformation at 300–400 °C, Al–0.06Sc–0.06Zr exhibits threshold stresses of 7–12 MPa; these values may be further improved by optimal heat-treatments.
Published by Elsevier Ltd. on behalf of Acta Materialia Inc.

Keywords: Aluminum alloys; Precipitation; Isochronal heat-treatments; Scandium; Zirconium

1. Introduction

The Al–Zr system shows particular promise for developing creep-resistant, thermally stable Al-based alloys at elevated temperatures [1,2]. During post-solidification aging, decomposition of supersaturated Al–Zr solid solutions occurs initially by the formation of nanometer-scale Al_3Zr precipitates with a metastable cubic $L1_2$ structure, which transform to the equilibrium $D0_{23}$ phase after prolonged aging at elevated temperatures (>450 °C) [3–11]. The stability of the $L1_2$ metastable phase at high homologous temperatures is attributed to the slow diffusion kinetics of Zr in α-Al and a small lattice parameter mismatch of Al_3Zr ($L1_2$) with α-Al [1].

In previous studies by the authors, the microstructures and ambient-temperature mechanical properties of conventionally solidified Al–Zr alloys were studied during isothermal aging at 375, 400, 425 °C [12] and 500 °C [13] or during isochronal aging up to 600 °C [13]. Precipitation of spheroidal, nanometer-scale Al_3Zr ($L1_2$) precipitates results in a pronounced hardening response at all aging temperatures investigated. There is no appreciable overaging effect despite extended aging times (3200 h) at 425 °C ($0.75T_m$, where T_m is the absolute melting temperature of Al) [12], and only at or above ~475 °C do the metastable $L1_2$ trialuminide precipitates transform to their equilibrium $D0_{23}$ structures [13].

The Al_3Zr precipitates are, however, heterogeneously distributed (Fig. 1), reflecting the dendritic microsegregation

* Corresponding author at: US Naval Research Laboratory, Multifunctional Materials Branch, Washington, DC 20375-0001, USA. Tel.: +1 202 767 2947.
E-mail address: keith.knipling@nrl.navy.mil (K.E. Knipling).
URLs: http://arc.nucapt.northwestern.edu (D.N. Seidman), http://dunand.northwestern.edu (D.C. Dunand).

1359-6454/$36.00 Published by Elsevier Ltd. on behalf of Acta Materialia Inc.
doi:10.1016/j.actamat.2010.10.017

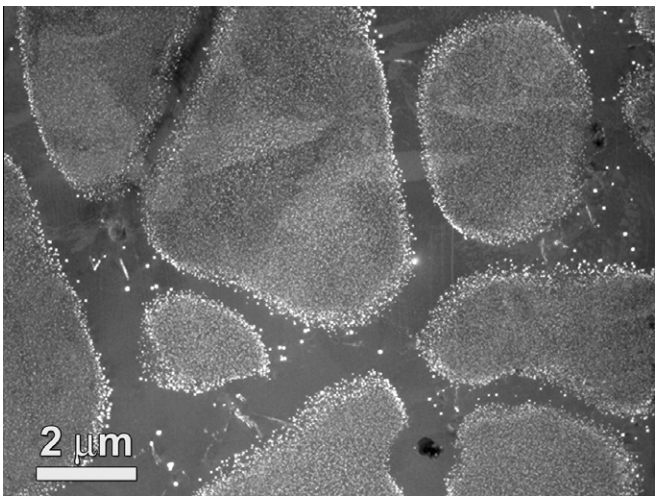

Fig. 1. Centered dark-field transmission electron micrograph of an Al–0.1Zr–0.1Ti (at.%) alloy aged at 375 °C for 1600 h, exhibiting an inhomogeneous dendritic distribution of 3–5-nm-radius $Al_3(Zr_{1-x}Ti_x)$ ($L1_2$) precipitates [12].

of Zr solute atoms during solidification [12]. Because Zr forms a terminal peritectic with Al, the liquidus and solidus boundaries of the α-Al solid solution plus liquid two-phase region have positive slopes and k_0, the equilibrium partition coefficient for solidification, is greater than unity. The first solid to form during solidification is therefore richer in Zr compared to the bulk alloy composition, resulting in solute-rich dendritic cells surrounded by solute-depleted interdendritic channels. Upon aging, only the enriched dendritic cells are sufficiently supersaturated to cause precipitation of Al_3Zr. The precipitate-free interdendritic channels have a deleterious effect on the mechanical properties, both at ambient temperature [1,3,15–19] and during creep experiments performed at 300, 350 or 400 °C [14]. Precipitation strengthening in these alloys occurs on multiple length scales: (i) on the nanometer-scale scale by a shearing or Orowan precipitation strengthening mechanism; and (ii) on the micrometer-scale related to the volume fraction of the precipitate-rich dendrites [13].

Dendritically distributed Al_3Zr ($L1_2$) precipitates are also a significant problem in commercial wrought alloys, where Zr is added as a recrystallization inhibitor [1,3,15–19]. During solutionizing, which is typically performed at ~500 °C coherent Al_3Zr ($L1_2$) precipitates are formed, which inhibit subsequent recrystallization by pinning migrating grain boundaries, thus maintaining grain boundary strengthening. The alloys are prone to recrystallization, however, in the interdendritic regions, where the number density of Al_3Zr precipitates is small [20–23]. Several recent studies have aimed to minimize the extent of the precipitate-free interdendritic regions through multi-step annealing procedures [20,24,25] and other alloying additions, including Cu, Mg, Zn [21,26], Si, Fe, Mn [23,27] and Sc [22,27–33] in 7xxx and other commercial wrought alloys.

There is a particularly strong interest in adding Sc to improve the precipitate distribution, thereby improving recrystallization resistance of Al–Zr alloys [22,27–34]. Robson [31] and Forbord et al. [27] have demonstrated that by combining Sc, a solute forming a terminal eutectic with Al ($k_0 < 1$), with Zr, a peritectic solute ($k_0 > 1$), the precipitate-free regions associated with a Sc-free alloy may be eliminated. Their argument, supported by experimentally measured solute concentration profiles, is that during solidification Zr and Sc solute atoms segregate at the dendrite interiors and exteriors, respectively, effectively "filling in" the interdendritic regions with Sc, which forms Al_3Sc ($L1_2$) precipitates upon subsequent thermal aging. A similar effect has also been observed by Lieblich and Torralba [35,36] with Al–Li–Ti alloys, where Ti (a peritectic-forming solute) segregates to the dendrite interiors and Li (a eutectic-forming solute) segregates to the peripheries. A further advantage of combining Zr and Sc is the improved coarsening resistance of $Al_3(Sc_{1-x}Zr_x)$ ($L1_2$) precipitates compared with Al_3Sc ($L1_2$) [37–42]. Finally, first-principles calculations show that Sc should stabilize the $L1_2$ structure of Al_3Zr [43], which may delay their transformation to the equilibrium $D0_{23}$ structures.

We previously investigated precipitation strengthening in binary Al–0.1Sc, Al–0.1Zr and ternary Al–0.1Sc–0.1Zr (at.%) alloys aged isochronally from 200 to 600 °C [42]. Precipitate compositions, mean radii ($\langle R \rangle$) and volume fractions (ϕ) were measured in the Al–Sc–Zr alloy using atom-probe tomography (APT), and were used to identify and quantify the observed strengthening increments due to the resistance to shear of the $Al_3(Sc_{1-x}Zr_x)$ ($L1_2$) precipitates. The Al–Sc–Zr alloy, however, contained primary $Al_3(Sc_{1-x}Zr_x)$ precipitates formed during solidification, resulting in a fine-grained microstructure (~50 μm grain diameter), which is unsuitable for creep resistance. In this article, we investigate the as-cast solute microsegregation, ambient-temperature microhardness and high-temperature creep resistance in more dilute, coarse-grained Al–0.06Sc, Al–0.06Zr and Al–0.06Sc–0.06Zr (at.%) alloys.

2. Experimental procedures

2.1. Alloy compositions and preparation

Binary Al–0.06Sc and Al–0.06Zr alloys and a ternary Al–0.06Sc–0.06Zr alloy were investigated; alloy designations and exact compositions are summarized in Table 1 (all compositions are in at.% unless otherwise noted). Small

Table 1
Compositions of the Al–Sc, Al–Zr and Al–Sc–Zr alloys investigated (at.%).

Alloy	Nominal comp.		Verified comp.[a]	
	Sc	Zr	Sc	Zr
Al–0.06Sc	0.06	–	0.062	–
Al–0.06Zr	–	0.06	–	0.059
Al–0.06Sc–0.06Zr(a)	0.06	0.06	0.057	0.059
Al–0.06Sc–0.06Zr(b)	0.06	0.06	0.074	0.077

[a] As measured by direct-current plasma emission spectroscopy.

(~7 g) buttons were prepared by melting 99.95 at.% Al (Atlantic Equipment Engineers, Bergenfield, NJ) with a dilute Al–0.12Sc master alloy (Ashurst Technology, Ltd., Baltimore, MD) and/or an Al–0.57Zr master alloy, employing non-consumable electrode arc-melting in a gettered purified-argon atmosphere. The pure Al contained 260 at. ppm Fe and 260 at. ppm Si as impurities, as determined by glow-discharge mass spectrometry (Shiva Technologies/Evans Analytical Group, Syracuse, NY). The Al–0.57Zr master alloy was dilution cast from a commercial 10 wt.% Zr master alloy (KB Alloys, Reading, PA). The verified compositions in Table 1 were obtained by bulk chemical analysis performed by direct current plasma emission spectroscopy (ATI Wah Chang, Albany, OR).

Except for the Al–Sc binary alloy, the alloys were not homogenized prior to isochronal aging. This is because Al–Zr alloys, with sufficient Zr concentrations for appreciable precipitation strengthening, form coarse Al_3Zr precipitates at the homogenization temperature, resulting in minimal precipitation hardening during subsequent aging (as discussed in detail below). The Al–Sc–Zr castings were intentionally left in their as-cast state to take advantage of the expected segregation of Sc at the Zr-poor dendrite peripheries. The Al–Sc alloy was studied in both the as-cast and homogenized states; homogenization was carried out at 640 °C for 28 h.

Two button ingots of Al–0.06Sc–0.06Zr, labeled (a) and (b), were prepared to ensure that sufficient material was available for subsequent analyses. Most analyses were performed on Al–0.06Sc–0.06Zr(a), which was aged to only 400 °C to preserve the bulk of the material in the peak-aged condition and to allow for subsequent isothermal aging. Likewise, the as-cast specimen of Al–0.06Sc was aged to only 400 °C, while the homogenized specimen was aged to 500 °C.

2.2. As-cast microstructural analysis

The microstructures of the as-cast specimens were observed utilizing optical microscopy and scanning electron microscopy (SEM). The initial solute distribution was measured in as-cast specimens by quantitative electron-probe microanalysis (EPMA) using a Cameca SX50 electron-probe microanalyzer operating at 15 kV and 20 nA equipped with four wavelength dispersive spectrometers (WDSs). The reported uncertainty is one standard deviation of the analytical sensitivity.

2.3. Aging treatments, Vickers microhardness and electrical conductivity

The alloys were aged isochronally in 25 °C increments, each lasting 3 h, beginning at 200 °C and terminating at 600 °C. After each aging step, the specimens were water-quenched and precipitation was monitored by Vickers microhardness and electrical conductivity measurements. The Vickers microhardness measurements were performed at ambient temperature on metallographically polished sections using a load of 200 g and a dwell time of 5 s. A minimum of 20 microhardness measurements were recorded for each temperature. The electrical conductivity measurements were performed at ambient temperature using an eddy current apparatus (Sigmatest 2.069 from Foerster Instruments, Pittsburgh, PA), placing the contact probe on a clean, planar surface. Five electrical conductivity measurements were recorded on each specimen, each reading corresponding to a different frequency (60, 120, 240, 480 or 960 kHz), and the mean value is reported. For consistency, a single specimen of each alloy was used for the electrical conductivity measurements, which was measured between each isochronal aging step. An increase of electrical conductivity corresponds to a decrease in the supersaturation of Sc and Zr in the matrix due to an increasing value of ϕ [44–48]. Uncertainty in both measurements is reported as one standard deviation from the mean.

2.4. Creep experiments

Specimens of Al–0.06Sc–0.06Zr(a), peak-aged isochronally to 400 °C, were tested by creep. Creep specimens in the shape of parallelepipeds (~$4 \times 4 \times 8$ mm^3) were electrode-discharge machined with their axes perpendicular to the surface of the ingot that had been in contact with the water-cooled copper crucible during arc-melting. The length of the creep specimen spans almost the entire height of the button ingot. The specimens were aged prior to machining.

A superalloy creep cage translated tensile loads in the pull-rods to compressive stresses on the specimen. Frictional effects on the end-loaded specimens were minimized using alumina platens coated with boron nitride. Specimen temperature was measured in the three-zone furnace with a temperature stability of ±1 °C after a 1 h soak at the test temperature. Specimen strain was calculated from extensometric displacements of cage platens measured using a linear variable differential transducer (LVDT) with a resolution of 2.5 μm. Once steady-state deformation was achieved, the load was increased, resulting in three to five data points suitable for determining a stress exponent from one specimen; total specimen strain did not exceed 10%.

3. Results

3.1. As-cast microstructure

The as-cast macrostructures of the alloys are typical of conventionally solidified alloys, exhibiting coarse (millimeter-scale) columnar grains. No primary precipitates were observed in any of the alloys. The as-cast solute microsegregation was determined by measuring linear concentration profiles utilizing EPMA (Fig. 2) for the Al–0.06Sc (both as-cast and homogenized), Al–0.06Zr

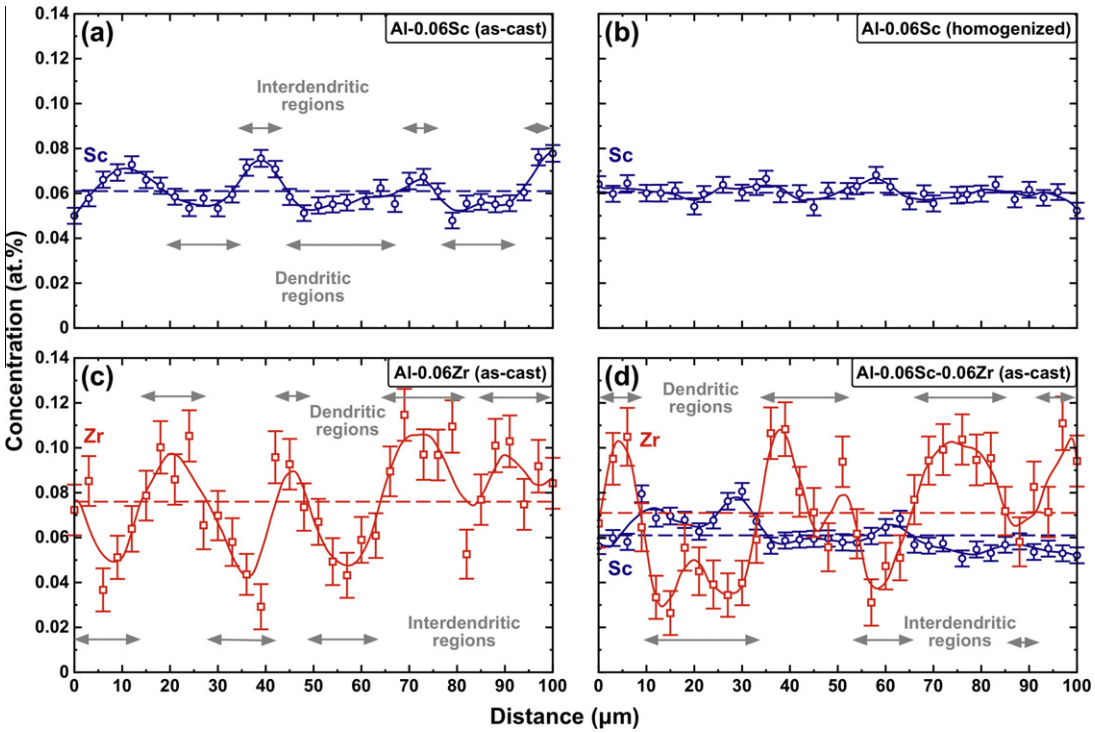

Fig. 2. Concentration profiles of Sc and Zr, measured by EPMA, across multiple dendritic cells in: (a) as-cast Al–0.06Sc; (b) homogenized Al–0.06Sc; (c) as-cast Al–0.06Zr; and (d) as-cast Al–0.0Sc–0.066Zr(a).

and Al–0.06Sc–0.06Zr(a) alloys. Each 100-μm-long analyzed traverse spans multiple dendritic cells in each alloy, as evidenced by the periodic variations in solute concentration. The horizontal dashed lines indicate the mean measured solute concentrations for each set of data.

In as-cast Al–0.06Sc (Fig. 2a) the dendritic cells contain ~0.05 at.% Sc, (*i.e.* a depletion of ~0.01 at.% Sc below the measured mean Sc concentration of 0.061 ± 0.008 at.% Sc), whereas the interdendritic regions are enriched up to ~0.08 at.% Sc. The wavelength of the variations, which corresponds to the secondary dendrite arm spacing, is ~30 μm. After homogenization (Fig. 2b) there is no apparent variation in Sc concentration across the 100-μm-long scan, indicating that the homogenization treatment (640 °C for 28 h) has successfully eliminated the as-cast microsegregation of Sc. In both the as-cast and homogenized states, the measured mean Sc concentration (0.061 ± 0.008 and 0.060 ± 0.004 at.% Sc, respectively) is very near the bulk alloy composition of 0.062 at.% Sc (Table 1).

In as-cast Al–0.06Zr (Fig. 2c) the variations in Zr concentrations are much greater. Here, the Zr concentration varies by ~0.03 at.% above and below the measured mean value of 0.076 ± 0.022 at.% Zr. This mean Zr concentration is also significantly greater than the bulk composition of 0.059 at.% Zr (Table 1). The Zr-rich dendritic cells and the Zr-poor interdendritic regions are each ~10–15 μm across, which is comparable to the wavelength of the concentration variation observed in the as-solidified Al–Sc alloy (Fig. 2a).

In as-cast Al–0.06Sc–0.06Zr (Fig. 2d) the dendrites are enriched in Zr and concomitantly depleted in Sc. Scandium atoms are concentrated in the last solid to form, where the concentration is ~0.075–0.080 at.% Sc (*i.e.* 0.015–0.020 at.% Sc greater than the measured mean concentration of 0.061 ± 0.008 at.% Sc). Near the dendrite centers, the first solid to form, the concentration is ~0.05 at.% Sc (*i.e.* ~0.01 at.% below the mean value). This distribution of Sc is comparable to what is observed in the binary as-cast alloy (Fig. 2a). Zirconium segregates more strongly, varying by ~0.04 at.% about the measured mean concentration of 0.071 ± 0.026 at.% Zr, which is comparable to what is observed in the binary Al–Zr alloy (Fig. 2c). The wavelength of the solute concentration variations is the same as before, *i.e.*, 20–30 μm.

The measured mean Sc concentrations in Fig. 2a, b and d agree very well with bulk alloy compositions in Table 1, while the measured concentrations in the Zr-containing alloys, Fig. 2c and d, both exhibit an apparent enrichment in Zr. It is possible that this enrichment could represent a macrosegregation of Zr between the 100-μm-long locally sampled regions of the alloys. The two castings exhibit a similar bias suggesting that the apparent enrichment of Zr may also be an artifact of the EPMA technique.

3.2. Vickers microhardness and electrical conductivity

Fig. 3 displays the precipitation behavior of Al–0.06Sc, Al–0.06Zr and Al–0.06Sc–0.06Zr during isochronal aging,

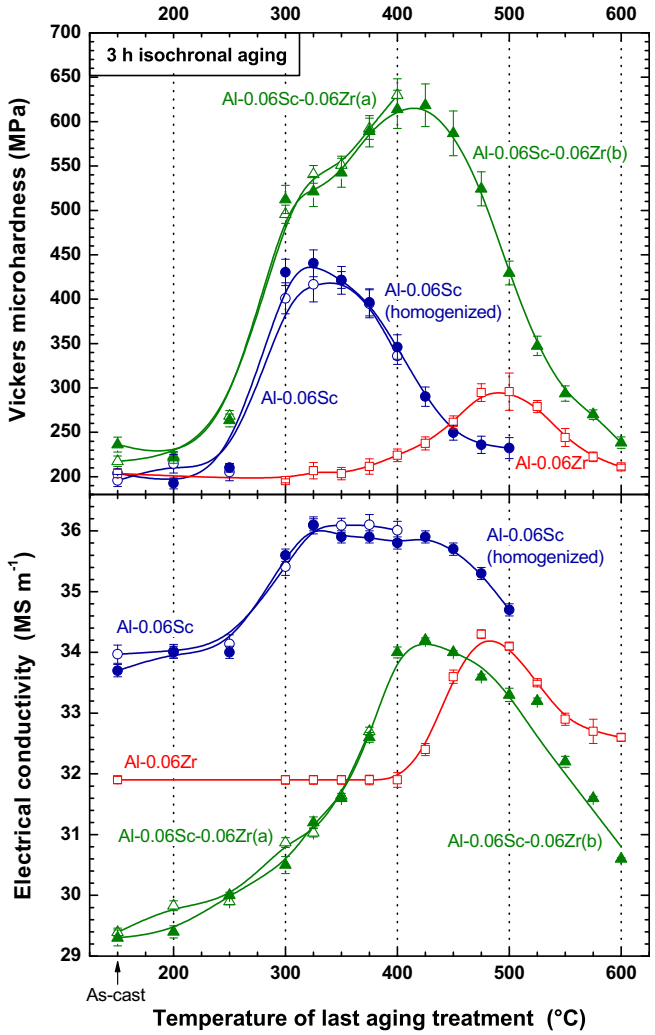

Fig. 3. Vickers microhardness and electrical conductivity evolution during isochronal aging (3 h at each temperature) of Al–0.06Sc, Al–0.06Zr and Al–0.06Sc–0.06Zr alloys.

as monitored by Vickers microhardness and electrical conductivity measurements. Precipitation of Al_3Sc ($L1_2$) commences between 250 and 300 °C in the binary Al–Sc alloy, as evidenced by the increase in strength and the accompanying change in electrical conductivity, achieving a peak microhardness value of 429 ± 25 MPa at 325 °C, Peak electrical conductivity, which corresponds to a maximum ϕ value of Al_3Sc precipitates, also occurs at 325 °C. The change in electrical conductivity between the as-cast and maximum value is 2.2 ± 0.2 MS m^{-1}. There is a continuous decrease in microhardness above 325 °C, while the electrical conductivity remains near its peak value up to 425 °C. Homogenizing prior to aging has no effect on the observed microhardness or electrical conductivity, which is consistent with our previous observations on Al–0.1Sc alloys aged isochronally [42] and also concurs with the findings of Drits et al. [49] on Al–0.12Sc and Al–0.30Sc alloys aged isothermally at 350 °C.

In the Al–0.06Zr alloy, precipitation of Al_3Zr ($L1_2$) commences between 400 and 425 °C and leads to a peak microhardness value of 295 ± 10 MPa at 475 °C, with a corresponding change in electrical conductivity of 2.4 ± 0.1 MS m^{-1}. There is a continuous decrease in microhardness and electrical conductivity above 500 °C.

The as-cast electrical conductivity of Al–0.06Sc–0.06Zr (29.3 ± 0.1 MS m^{-1}) is significantly less than that of Al–0.06Sc (33.9 ± 0.2 MS m^{-1}) or Al–0.06Zr (31.9 ± 0.1 MS m^{-1}) because the ternary alloy contains nominally twice the amount of solute as the binary alloys. The as-cast microhardness of Al–0.06Sc–0.06Zr is also ~20–30 MPa greater than that of the binary alloys, which is attributable to solid solution strengthening from the larger solute concentration.

Upon aging, precipitation strengthening of Al–0.06Sc–0.06Zr parallels that of Al–0.06Sc up to 325 °C, with a comparable change in electrical conductivity (1.8 ± 0.2 MS m^{-1}), suggesting that a similar ϕ value of the precipitates is generated for both alloys. The nucleation kinetics of Al–0.06Sc–0.06Zr are accelerated slightly compared with those of Al–0.06Sc; at 250 °C Al–0.06Sc–0.06Zr has a microhardness value ~265 MPa, which is ~60 MPa greater than that of Al–0.06Sc. Furthermore, the electrical conductivity of Al–0.06Sc has not changed significantly at 250 °C, indicating the precipitation of Al_3Sc has not commenced in the Al–Sc alloy.

The Al–0.06Sc alloy achieves a peak microhardness at 325 °C, while Al–0.06Sc–0.06Zr experiences additional precipitate nucleation and growth, as evidenced by the continued increases in microhardness and electrical conductivity above 325 °C. Peak microhardness and electrical conductivity values of 618 ± 24 MPa and 34.2 ± 0.1 MS m^{-1}, respectively, are achieved at 425 °C, corresponding to a maximum ϕ value of $Al_3(Sc_{1-x}Zr_x)$ precipitates. There is a rapid decrease in microhardness and electrical conductivity above 425 °C, which indicates that significant $Al_3(Sc_{1-x}Zr_x)$ precipitate dissolution is occurring. Additions of Zr delay overaging by 100–125 °C as compared with the Al–Sc alloy.

3.3. Isothermal aging at 400 °C

Specimens of Al–0.06Sc–0.06Zr(a) aged isochronally to 400 °C (near peak microhardness; Fig. 3) were subsequently annealed isothermally at 400 °C for 400 h to assess their stability for extended high-temperature usage. Fig. 4 displays Vickers microhardness as a function of exposure time at 400 °C. A small decrease in microhardness (from its peak value of 630 ± 18 MPa) is first observed after 100 h at 400 °C, where the microhardness has decreased slightly to 605 ± 24 MPa; after 400 h, the microhardness has decreased further to 545 ± 13 MPa.

Data from our previous study on more concentrated Al–0.1Sc and Al–0.1Sc–0.1Zr alloys [42] are also displayed in Fig. 4 for comparative purposes. Because of the larger solute content, Al–0.1Sc–0.1Zr is initially much stronger (by ~110 MPa) than the Al–0.06Sc–0.06Zr alloy, but it also overages at a faster rate, such that both alloys exhibit

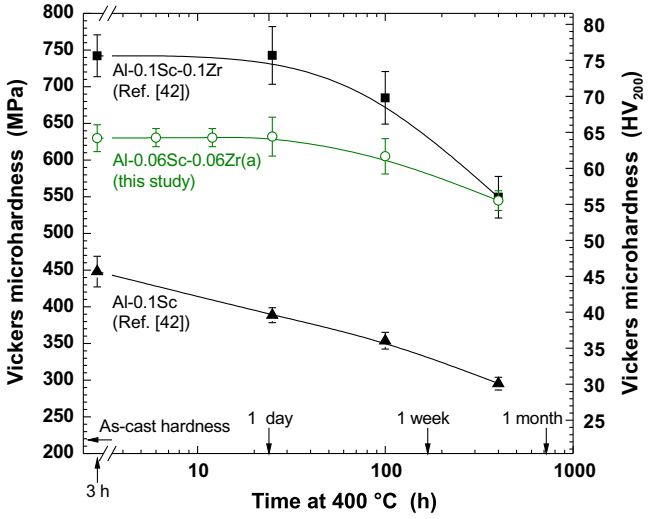

Fig. 4. Vickers microhardness vs. time at 400 °C for Al–0.06Sc–0.06Zr(a), after aging isochronally to 400 °C to achieve peak microhardness (Fig. 3). The closed symbols represent data for Al–0.1Sc and Al–0.1Sc–0.1Zr alloys from Ref. [42].

comparable microhardness values after 400 h at 400 °C. During isochronal aging to 400 °C Al–0.1Sc is already overaged considerably from its peak microhardness value of 668 ± 20 MPa (which occurs at 325 °C) to 448 ± 21 MPa at 400 °C [42]. This alloy continues to overage isothermally at 400 °C, achieving a microhardness of 295 ± 9 MPa after 400 h. The present Al–0.06Sc–0.06Zr alloy is thus significantly stronger than Al–0.1Sc, despite its smaller Sc concentration.

3.4. Creep at 300–400 °C

During high-temperature loading, a primary creep regime, where the strain rate decreases continuously with time, always precedes steady-state creep. The minimum strain rate from the steady-state regime, $\dot{\epsilon}$, is plotted as a function of applied stress in Fig. 5 for tests performed at 300, 350 or 400 °C. The Al–0.06Sc–0.06Zr alloy exhibits creep resistance in the low stress regime where the apparent stress exponent, n (given by the slope of the double logarithmic plot in Fig. 5), is much greater than that for pure Al. This is indicative of the existence of a threshold stress, σ_{th}, below which creep deformation is not measurable. The minimum strain rate can thus be described by a modified power-law equation:

$$\dot{\epsilon} = A(\sigma - \sigma_{th})^n \exp\left(-\frac{Q}{R_g T}\right) \quad (1)$$

where A is a constant, σ is the applied stress, Q is an activation energy, R_g is the ideal gas constant and T is the absolute temperature. Values of σ_{th} were calculated from the data in Fig. 5 employing a linear weighted least-squares regression of $\dot{\epsilon}^{1/n}$ vs. σ [50] using $n = 4.4$ [51] for dislocation creep of Al. At 300, 350 and 400 °C values of $\sigma_{th} = 12$, 9 and 7 MPa, respectively, are determined.

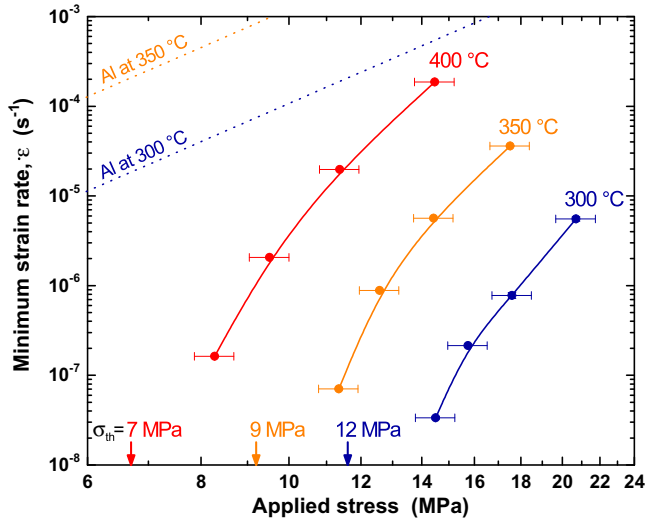

Fig. 5. Double logarithmic plot of minimum creep rate at 300, 350 or 400 °C vs. applied compressive stress for Al–0.06Sc–0.06Zr(a) aged isochronally to 400 °C (peak microhardness). The arrows indicate calculated values of the threshold stress.

4. Discussion

4.1. As-cast microstructure

Scandium forms a terminal eutectic with Al while Zr forms a terminal peritectic [1]. The eutectic composition in the Al–Sc system, which corresponds to the minimum solubility of Al_3Sc in liquid Al, is 0.28 at.% Sc [1,52,53]. The peritectic liquid composition [54] in the Al–Zr system, which corresponds to the minimum solubility of Al_3Zr in liquid Al, is 0.033 at.% Zr [1,55]. Thus, for the present alloys containing ~0.06 at.% Sc and/or Zr, primary Al_3Zr precipitates are thermodynamically possible but primary Al_3Sc precipitates are not. Even when exceeding their minimum solubility, however, primary precipitates can be suppressed kinetically during solidification. For a given solidification rate, there is a corresponding critical solute concentration below which primary precipitation of Al_3M (M = Sc and/or Zr) will not occur [1,2,54,56,57]. This phenomenon has been studied in detail for the Al–Zr system by Ohashi and Ichikawa [58] and Hori et al. [59,60] over a wide range of solidification rates (10^0–10^7 °C s^{-1}) and Zr concentrations (0.01–1.0 at.% Zr). Their findings indicate that primary Al_3Zr precipitates are suppressed in alloys containing less than ~0.1–0.2 at.% Zr, even at the slowest solidification rates investigated. These results are in agreement with our prior study on arc-melted Al–0.1Zr and Al–0.2Zr alloys solidified under identical conditions as the present alloys, where primary Al_3Zr precipitates were observed in Al–0.2Zr but not in Al–0.1Zr [12].

The situation is more complex for ternary alloys, however. We observed copious precipitation of primary $Al_3(Sc_{1-x}Zr_x)$ precipitates in arc-melted Al–0.1Sc–0.1Zr, despite that ~0.1 at.% Zr content in the alloy [42]. The primary precipitates have several undesirable consequences.

The amount of solute retained in solid solution is decreased, thus limiting the potential for precipitation strengthening during post-solidification aging. The maximum microhardness observed in Al–0.1Sc–0.1Zr was ~780 MPa (~150 MPa larger than that observed in the present Al–0.06Sc–0.06Zr alloy; Fig. 3), which would have been even greater had the formation of primary $Al_3(Sc_{1-x}Zr_x)$ been suppressed. The primary precipitates also act as heterogeneous nuclei during solidification of the melt, resulting in a fine-grained microstructure that is unsuitable for creep resistance. The optimum composition for a creep-resistant Al–Sc–Zr alloy with a Sc:Zr ratio of unity is thus between Al–0.06Sc–0.06Zr and Al–0.1Sc–0.1Zr.

Solidification is a first-order phase transformation involving a discontinuous change in the equilibrium atomic fractions of solute in the liquid and solid phases, as conveyed quantitatively by the solidus and liquidus curves in the phase diagram. The equilibrium solid–liquid partition coefficient, $k_0 = C_S/C_L$, quantifies the difference in the compositions of the solid (C_S) and liquid (C_L) phases in local equilibrium during solidification [61–63]. Assuming that the liquidus and solidus curves are linear, k_0 is estimated from the equilibrium binary phase diagrams as 0.8 for Al–Sc and 2.5 for Al–Zr [1].[1]

Because the composition of the solid differs from that of the liquid in equilibrium with it, solute redistribution occurs on the scale of the dendrite arm spacing. Assuming complete mixing in the liquid and negligible diffusion in the solid, then C_S is given by the Scheil equation:

$$C_s = k_0 C_0 (1 - f_S)^{k_0 - 1} \quad (2)$$

where C_0 is the bulk alloy composition and f_S is the fraction solidified.

Fig. 6 displays the Sc or Zr concentration as a function of f_S for the solidification of binary Al–0.06Sc and Al–0.06Zr alloys, as predicted by Eq. (2). For the Al–0.06Sc alloy, the first solid to form is depleted in Sc relative to bulk composition ($k_0 C_0 = 0.048$ at.% Sc) and Sc is continually rejected until the last liquid to solidify has the eutectic composition of 0.28 at.% Sc. Because the alloy is so dilute, Eq. (2) predicts a negligible amount of eutectic constituent formed ($f_S < 0.0002$), which is consistent with the absence of Al_3Sc precipitates in the as-cast alloys. For Al–0.06Zr, the first solid to form is enriched in Zr ($k_0 C_0 = 0.15$ at.% Zr) and Al is rejected until the last solid to form is essentially Zr-free.

We now compare the relative fractions of the alloys that are enriched ($C_S > C_0$) or depleted ($C_S < C_0$) with respect to their overall bulk compositions. For Al–0.06Sc, Fig. 6 predicts that $C_S < C_0$ for most of the solid ($f_S < 0.67$).

[1] The partition coefficient, k_0, is ordinarily defined where the compositions are in wt.%. To maintain consistency and to simplify the discussion, however, we calculate and apply k_0 using compositions in at.%. Furthermore, the difference between k_0 calculated with compositions in wt.% or at.% are negligible for the dilute concentrations considered here.

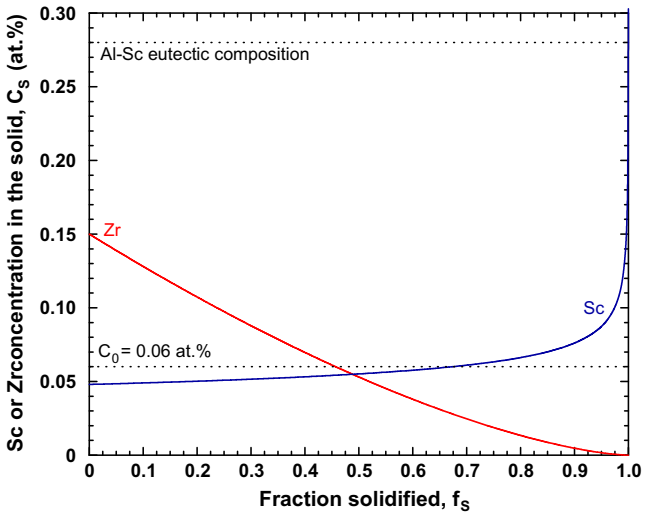

Fig. 6. Calculated as-cast solute distributions using the Scheil model, Eq. (2), for Al–0.06Sc and Al–0.06Zr.

The degree of this depletion is modest, however, by ~0.01 at.% Sc. For the remaining solid ($f_S > 0.67$) with $C_S > C_0$, the enrichment is not significant until $f_S \to 1$. This is in reasonable agreement with our observations of the as-cast alloy (Fig. 2a), where the Sc-depleted dendritic regions are wider than the Sc-enriched interdendritic regions and the Sc concentration varies slightly (between ~0.05 and ~0.08 at.% Sc). The relatively uniform distribution of Sc atoms after solidification is expected to lead to a somewhat homogeneous distribution of Al_3Sc precipitates after aging, which explains why the precipitation strengthening behavior of both the as-cast and homogenized Al–Sc specimens are identical in Fig. 3 and in our previous study [42].

For Al–Zr, Fig. 6 predicts that $C_S > C_0$ for almost half of the solid ($f_S < 0.46$). This agrees with the experimental data in Fig. 2c, where approximately half of the alloy is enriched above the measured C_0 value, while the other half is depleted. The measured Zr concentration variations are also much larger than those for Sc (Fig. 2), which is consistent with the predicted behavior (Fig. 6). The measured concentration profiles in Fig. 2 also concur with Sc and/or Zr solute microsegregation previously measured in commercial 7xxx alloys by EPMA [23,27,29,31].

In the Zr-containing alloys (Fig. 2c and d), the minimum measured Zr concentration is ~0.04 at.% whereas, according to Fig. 6, the Zr concentration in the interdendritic solid should approach 0. We observed a systematic enrichment in the Zr concentration by ~0.01 at.% Zr (Fig. 2c and d), which may explain why the concentration of Zr measured in the interdendritic regions is greater than expected. While this could be attributable to macrosegregation of Zr, the fact that both concentration profiles (taken from two separate ingots) exhibit a similar bias suggests that this may be an artifact of the EPMA technique. We have previously measured as-cast concentration profiles in similar Al–0.1Zr and Al–0.2Zr alloys using energy-dispersive X-ray

spectroscopy, and observed that the dendrite centers are enriched nearly twofold in Zr while the interdendritic regions are virtually Zr-free, in agreement with Fig. 6 [12,64].

Homogenizing the Al–0.06Sc alloy at 640 °C for 28 h eliminates the as-cast microsegregation of Sc (Fig. 2a and b). In dendritically solidified alloys, the homogenization time required to reduce the amplitude of the solute concentration variation to 5% of its initial value is [65]:

$$t_{0.05} \cong 0.3\frac{\lambda^2}{D} \tag{3}$$

where λ is the secondary dendrite arm spacing and D is the solute diffusivity. Fig. 2a indicates that $\lambda \sim 30$ μm; $D = D_0\exp(-Q/R_gT)$, where $Q = 173$ kJ mol^{-1} and $D_0 = 5.31 \times 10^{-4}$ m^2 s^{-1} for diffusion of Sc in α-Al [1,66] and at 640 °C $D = 6.7 \times 10^{-14}$ m^2 s^{-1} and Eq. (3) predicts $t_{0.05} = 4.0$ ks (1.1 h). The 28 h homogenization treatment employed for Al–0.06Sc is sufficient for removing the as-cast Sc segregation, which is consistent with the measured concentration profiles (Fig. 2b).

The Al–Zr alloy was not homogenized because the attainable microhardness during subsequent aging was reduced significantly [67]. This can be understood by considering the solid solubility of Zr in α-Al and the calculated as-cast Zr microsegregation profile (Fig. 6), and the measurement results (Fig. 2). The metastable ($L1_2$) and stable ($D0_{23}$) Al_3Zr solvus curves have been determined by *ab initio* calculations [68] and at 640 °C, the homogenization temperature employed for the Al–Sc alloy, the calculated solubilities are 0.233 and 0.071 at.% Zr, respectively. Fig. 6 demonstrates that a significant fraction of the alloy ($f_S \leqslant 0.39$) is supersaturated above 0.071 at.% Zr, suggesting that Al_3Zr ($D0_{23}$) precipitates would be nucleated in those regions during homogenization, thereby reducing the amount of Zr in solid solution available for precipitation during subsequent aging. Jia et al. [23] observed similarly that homogenizing an Al–0.04Zr–0.50Mn alloy at 630 °C decreased the number density of Al_3Zr precipitates during subsequent precipitation aging.

The Al–Sc–Zr alloys were not homogenized to preserve the microsegregation of Sc at the Zr-poor dendrite peripheries. Based on the as-cast solute concentration profile (Fig. 2d), it is expected that Al_3Zr ($D0_{23}$) would also be nucleated during homogenization, thereby limiting the potential for precipitation strengthening during aging.

4.2. Vickers microhardness and electrical conductivity

The nucleation and growth of Al_3Sc ($L1_2$) occurs at much lower temperatures than Al_3Zr ($L1_2$), which is partially reflective of the disparity in diffusivities between Sc and Zr in α-Al. For diffusion of Zr in α-Al, $Q = 242$ kJ mol^{-1} and $D_0 = 7.28 \times 10^{-2}$ m^2 s^{-1} [1,69]. Precipitation of Al_3Sc is detected first between 250 and 300 °C (Fig. 3), where the calculated diffusivity of Sc in α-Al is 0.3–9.0 × 10^{-20} m^2 s^{-1}. At 425 °C, where precipitation of Al_3Zr is first observed, the calculated diffusivity of Zr in α-Al is 5.6×10^{-20} m^2 s^{-1}. The peak microhardness temperatures are similarly shifted to higher temperatures: Al–0.06Sc reaches peak microhardness and conductivity at 325 °C, whereas this occurs between 475 and 500 °C for Al–0.06Zr. At 325 °C, the diffusivity of Sc in α-Al is 4.1×10^{-19} m^2 s^{-1}; a similar diffusivity for Zr occurs at 460 °C. The change in electrical conductivity between the as-cast and peak-aged conditions is comparable for Al–0.06Sc (2.1 ± 0.2 MS m^{-1}) and Al–0.06Zr (2.4 ± 0.1 MS m^{-1}), suggesting that a similar ϕ value of precipitates is formed in both alloys during aging; this assumes that the specific resistivities of Sc and Zr are similar. The peak microhardness, however, is much greater for Al–0.06Sc (429 ± 25 MPa) than it is for Al–0.06Zr (295 ± 10 MPa), as discussed further with Fig. 7 below.

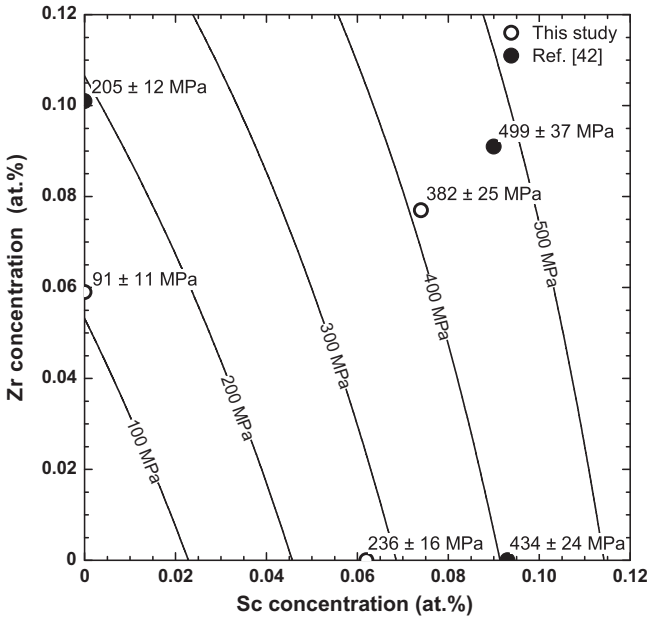

Fig. 7. Maximum microhardness increase achieved during isochronal aging of Al–Sc, Al–Zr and Al–Sc–Zr alloys. The data points are from this study and a prior one on more concentrated alloys [42]. The contour lines represent a quadratic response surface (Eq. (4)) fitted to the data.

There is a continuous decrease in microhardness of Al–0.06Sc above 325 °C, while the electrical conductivity remains near its peak value up to 425 °C, suggesting that the Al_3Sc precipitates are coarsening at a constant (maximum) ϕ value from 325 to 425 °C. Above 425 °C, the continuous decrease in electrical conductivity indicates that Al_3Sc precipitates are dissolving. The overaging of Al–0.06Sc for $T > 325$ °C is consistent with studies on similar conventionally solidified Al–Sc alloys, which are coarsening-resistant up to ~300 °C [37,49,70–74].

The overaging of Al–0.06Zr occurs at much higher temperatures, which is explained by the much smaller diffusivity of Zr in α-Al. Above 475 °C, there is a continuous decrease in microhardness with a concomitant diminution in electrical conductivity, which is due to coarsening and dissolution of the spheroidal Al_3Zr ($L1_2$) precipitates and their transformation to their equilibrium $D0_{23}$ structure [13].

The electrical conductivity of as-cast Al–0.06Sc–0.06Zr is much smaller than those of the binary Al–0.06Sc or Al–0.06Zr alloys, due to the larger solute concentrations in the ternary alloy. The change in electrical conductivity between the as-cast specimens and those aged to 325 °C is 1.6 ± 0.1 MS m^{-1} for Al–0.06Sc–0.06Zr(a) and 1.9 ± 0.2 MS m^{-1} for Al–0.06Sc–0.06Zr(b), which is slightly smaller than that of the binary Al–0.06Sc alloy over the same temperature range (2.1 ± 0.2 MS m^{-1}). This suggests that the precipitates formed up to 325 °C in the Al–Sc–Zr alloy contain little Zr, since there is no additional change in electrical conductivity as compared with the binary Al–Sc alloy. At 325 °C, Sc atoms ($D = 4.1 \times 10^{-19}$ m^2 s^{-1}) are significantly more mobile than Zr atoms ($D = 5.3 \times 10^{-23}$ m^2 s^{-1}), explaining why Zr atoms have not yet diffused to the precipitates.

Between 325 and 425 °C there is an additional increase in microhardness and electrical conductivity for Al–0.06Sc–0.06Zr, which is attributable to the diffusion of Zr to the already-nucleated Al_3Sc precipitates. The resulting $Al_3(Sc_{1-x}Zr_x)$ ($L1_2$) precipitates are thus enveloped in a Zr-enriched outer shell, which increases the ϕ value of the precipitates without diminishing their number density, thereby increasing the microhardness to its maximum value of 618 ± 24 MPa at 425 °C. We have quantified this strengthening effect using APT in a similar isochronal aging study of Al–0.1Sc–0.1Zr alloys [42]. Similar core–shell structure precipitates are well documented for Al–Sc–Zr alloys, as observed by APT [40,42,72–77], analytical high-resolution electron microscopy [76,78,79], small-angle X-ray scattering [76,80] and atomic-scale simulations [76,81]. The change in electrical conductivity from 325 to 425 °C (3.0 ± 0.1 MS m^{-1}) is greater than the change between the as-cast and peak-aged conditions for Al–0.06Zr (2.4 ± 0.1 MS m^{-1}), which suggests that some Sc, in addition to Zr, continues to precipitate out of solid solution over this temperature range. The total change in conductivity from the as-cast to peak-aged condition is 4.9 ± 0.1 MS m^{-1}, which is close to the sum of the differences for the binary alloys.

The microhardness and electrical conductivity evolution during isochronal aging corroborates our previous observations on more concentrated Al–0.1Sc, Al–0.1Zr and Al–0.1Sc–0.1Zr alloys [42]. Those alloys exhibited systematically larger peak microhardness values as compared with the present alloys, which is expected based on the larger solute concentrations and the corresponding larger ϕ values. The nucleation kinetics were also accelerated in the more concentrated alloys because the larger supersaturation increases the thermodynamic chemical driving force. For example, nucleation of Al_3Sc is observed between 250 and 300 °C in Al–0.06Sc (Fig. 3), whereas in Al–0.1Sc it occurs between 200 and 250 °C. Similarly, the precipitation of Al_3Zr is first observed between 400 and 425 °C in Al–0.06Zr, while it occurs between 350 and 375 °C in Al–0.1Zr.

The maximum microhardness increase (Fig. 3) as compared with the value of the as-cast specimens is 236 ± 16 MPa for Al–0.06Sc (homogenized), 91 ± 11 MPa for Al–0.06Zr, and 382 ± 25 MPa for Al–0.06Sc–0.06Zr(b). These data are displayed in Fig. 7 with results from our prior study of Al–0.1Sc, Al–0.1Zr and Al–0.1Sc–0.1Zr alloys [42]. A quadratic response surface, indicated by the contour lines in Fig. 7, has also been fit to these data and has the form:

$$\Delta\sigma = 4380 \cdot C_{Sc} + 1880 \cdot C_{Zr} - 10370 \cdot C_{Sc}C_{Zr} \quad (4)$$

where C_{Sc} and C_{Zr} are the Sc and Zr solute concentrations (in at.%) and $\Delta\sigma$ is the maximum increase in Vickers microhardness (in MPa). On a per atom basis, the maximum precipitation strengthening achieved by Sc additions alone (4380 MPa per at.%) is more than twice as large as that of Zr (1880 MPa per at.%).

In cast Al–Zr alloys the initial distribution of Zr solute atoms is highly segregated (Fig. 2 and Ref. [12]), leading to precipitate-free interdendritic channels that have a deleterious effect on ambient-temperature strength [13]. This explains why the strengthening effect of Zr is comparatively weak. Furthermore, Sc provides one of the highest strengthening increments per atomic percent of any alloying addition to Al [70,82], and has been estimated to increase the yield stress by 1000 MPa per at.% Sc, as measured in uniaxial tension tests by Drits et al. [49,70]. Using a conversion factor of $\frac{1}{3}$ between Vickers microhardness and strength [83], Eq. (4) predicts a strengthening increase of 1460 MPa per at.% Sc, which exceeds the previously reported value by ~50%. Drits et al. [70], however, determined their strengthening increment from an alloy that was aged isothermally at 250 °C for 200 h. Their data suggest that a larger yield stress increment might have been achieved by aging at a lower temperature, 200 °C, for longer periods of time (their specimen aged at 200 °C had not yet achieved peak strength after 200 h). Lower aging temperatures should increase ϕ, thereby producing a larger strength increase. Whereas Drits et al. determined their strengthening increment from a single alloy that was aged isothermally, ours was calculated from multiple specimens (two Al–Sc, two Al–Zr and two Al–Sc–Zr specimens) that were aged isochronally. Isochronal aging promotes greater strengthening since precipitates are nucleated at the lowest possible aging temperature, where the solute supersaturation and chemical driving force are greatest, resulting in (i) smaller precipitates, since the critical radius for nucleation is reduced; and (ii) a larger ϕ value of precipitates because of the lever rule. This further explains why our estimated strengthening increment for Sc additions is greater than the Drits et al. value.

4.3. Isothermal aging at 400 °C

The Al–Sc–Zr alloy achieves peak microhardness at 400 °C during isochronal aging (Fig. 3), but the $Al_3(Sc_{1-x}Zr_x)$ precipitates coarsen after extended exposure at this temperature (detectable at 100 h and pronounced at 400 h; Fig. 4). The overaging observed at 400 °C is consistent with prior studies on Al–Sc–Zr alloys aged isothermally between

300 and 500 °C [37,38,42], indicating that the threshold for long-term stability of $Al_3(Sc_{1-x}Zr_x)$ precipitates is ~400 °C. While detrimental to ambient-temperature strength, the coarsening observed at 400 °C could, however, be employed to improve the high-temperature creep resistance, as discussed below.

4.4. Ambient and high-temperature strengthening mechanisms

The peak microhardness of Al–0.06Sc–0.06Zr(a) is 630 ± 18 MPa after isochronal aging to 400 °C (Fig. 3), which corresponds to a strength increase of $\Delta\sigma = 138 \pm 7$ MPa (employing the $\frac{1}{3}$ factor between microhardness and strength [83]). When crept at 300, 350 or 400 °C, this alloy exhibits creep threshold stresses of $\sigma_{th} = 12$, 9 or 7 MPa, respectively (Fig. 5). Thus σ_{th} is a small fraction (5–10%) of the ambient-temperature strength increment $\Delta\sigma$.

At ambient temperature, precipitate shearing or precipitate bypass by dislocation looping can generally explain strength in precipitate-strengthened alloys in the absence of other strengthening mechanisms (*e.g.*, Hall–Petch strengthening, solid solution strengthening or strain hardening) [84–89]. For small mean precipitate radii, $\langle R \rangle$, the strength is controlled by dislocation shearing of precipitates, whereas the Orowan looping mechanism controls strength for larger $\langle R \rangle$. While $\langle R \rangle$ values were not measured in this study, we have measured $Al_3(Sc_{1-x}Zr_x)$ precipitates with $\langle R \rangle$ of 1.7 ± 0.7 nm in an Al–0.1Sc–0.1Zr alloy isochronally aged in an identical manner, and have confirmed that precipitate shearing is the operating strengthening mechanism for $\langle R \rangle < 3$ nm [42]. In the present Al–0.06Sc–0.06Zr alloys we expect $Al_3(Sc_{1-x}Zr_x)$ precipitates with similar $\langle R \rangle$ values, leading to similar shearing strengthening mechanisms.

At elevated temperatures, there is sufficient thermal energy to allow dislocations to circumvent the precipitates by climbing out of their glide plane. The increase in dislocation length during this process results in a threshold stress, $\Delta\sigma_{th}$ (which is linearly proportional to the Orowan stress, $\Delta\sigma_{or}$ [90–92]), below which creep deformation is not measurable. Elastic interactions due to elastic modulus and lattice parameter mismatches between the precipitates and matrix can further increase the creep $\Delta\sigma_{th}$ value for coherent precipitates, resulting in a rapid increase in σ_{th} with increasing $\langle R \rangle$ up to values as large as $\sim 0.5\Delta\sigma_{or}$, as modeled in Refs. [93,94] and observed in numerous Al–Sc-based alloys [39,73,74,95–98]. The threshold stress is thus a trade-off between the Orowan stress (which decreases with $\langle R \rangle$) and repulsive interactions from modulus and lattice parameter mismatches (which increase with $\langle R \rangle$), resulting in an optimum precipitate size for creep, which for these alloys is $\langle R \rangle \sim 10$ nm. Thus, while the $Al_3(Sc_{1-x}Zr_x)$ precipitates are of optimum size for ambient-temperature strength, they are too small for maximum creep resistance, $\Delta\sigma_{th}$.

We now compare our results to similar creep studies on dilute Al–Sc [71,73,74], Al–Sc–Zr [39] and Al–Sc–Ti [96,98] alloys. A meaningful comparison requires knowledge of the precipitates' $\langle R \rangle$ and ϕ values. As discussed, we assume that $\langle R \rangle \sim 2$ nm based on our previous study [42]. For a homogeneous alloy containing 0.12 at.% total solute (Sc + Zr), the equilibrium value of ϕ is 0.48%, using the lever rule and assuming negligible solubility at the aging temperature; this is a reasonable assumption since precipitates are nucleated at the lowest possible aging temperature during isochronal aging.

Marquis et al. [73,74] measured a threshold stress $\sigma_{th} = 8$ MPa in an Al–0.06Sc alloy (strengthened with Al_3Sc precipitates where $\langle R \rangle = 4.1$ nm and $\phi = 0.24\%$) crept at 300 °C. Coarsening the precipitates to $\langle R \rangle = 8.5$ nm increased σ_{th} to 19 MPa. In our Al–0.06Sc–0.06Zr alloy the value of σ_{th} (12 MPa) is comparable or smaller at 300 °C despite having twice the total solute content and hence twice the nominal ϕ of precipitates, which is probably due to the smaller $Al_3(Sc_{1-x}Zr_x)$ precipitates in the present alloys ($\langle R \rangle \sim 2$ nm). In a more concentrated Al–0.12Sc alloy Marquis et al. measured $\sigma_{th} = 14$ MPa (for $\langle R \rangle = 3.0$ nm and $\phi = 0.49\%$), which is slightly larger than the one observed here ($\sigma_{th} = 12$ MPa) and is consistent with their larger $\langle R \rangle$ value.

Fuller et al. [39] crept several Al–Sc–Zr alloys at 300 °C. In the alloy most similar to ours, Al–0.07Sc–0.02Zr, they measured $\sigma_{th} = 14$ MPa (for $Al_3(Sc_{1-x}Zr_x)$ precipitates with $\langle R \rangle = 2.3$ nm and $\phi = 0.38\%$) ,which is comparable to the performance of the present alloy at 300 °C. When coarsened to $\langle R \rangle = 8.7$ nm, σ_{th} increased to 20 MPa. A similar improvement would be expected for the present alloys after isothermal overaging to a larger precipitate radius optimal for creep resistance (*e.g.*, isothermally at 400 °C as in Fig. 4).

The creep performance at higher temperatures can be compared with recent studies by van Dalen et al. [98] on Al–0.06Sc–0.06Ti (containing $Al_3(Sc_{1-x}Ti_x)$ precipitates with $\langle R \rangle = 8.3$ nm and $\phi = 0.27\%$), where $\sigma_{th} = 15$ and 10 MPa at 350 and 400 °C, respectively. These threshold stresses are ~50% larger than what we observe at those temperatures.

5. Conclusions

We investigated the microstructure and mechanical properties of conventionally solidified Al–0.06Sc, Al–0.06Zr and Al–0.06Sc–0.06Zr (at.%) alloys, isochronally aged from 200 to 600 °C. The following results were obtained:

- The as-cast macrostructures of the Al–0.06Sc, Al–0.06Zr and Al–0.06Sc–0.06Zr alloys are typical of conventionally solidified alloys, with millimeter-scale columnar grains without primary Al_3Sc, Al_3Zr or $Al_3(Sc_{1-x}Zr_x)$ precipitates. In the as-cast alloys, Sc is concentrated at the dendrite peripheries while Zr is segregated at the dendrite cores. The degree of Zr

segregation is significantly more pronounced than that of Sc, consistent with the larger partition coefficient for Al–Zr. Homogenizing for 28 h at 640 °C eliminates the Sc microsegregation in Al–0.06Sc completely. Alloys containing Zr cannot be homogenized without first precipitating Al_3Zr.

- Precipitation of Al_3Sc ($L1_2$) commences between 200 and 250 °C in the Al–0.06Sc alloy, achieving a peak microhardness of 429 ± 25 MPa at 325 °C. In the Al–0.06Zr alloy, precipitation of Al_3Zr ($L1_2$) commences between 400 and 425 °C, achieving a peak microhardness of 295 MPa at 475–500 °C. The diffusivity of Sc in α-Al is significantly greater than that of Zr, which explains the faster precipitation kinetics for the Al–Sc alloy. On a per atom basis, Sc is a significantly more potent strengthener than Zr, probably because of the more pronounced segregation of Zr (Fig. 2) and the associated nonuniform precipitate distributions in the Al–Zr alloys (Fig. 1), which are known to be deleterious to strength [13].
- In the ternary Al–0.06Sc–0.06Zr alloy, the precipitation strengthening behavior parallels that of Al–0.06Sc up to 325 °C. At higher temperatures, Zr additions result in a secondary strength increase, attaining a peak Vickers microhardness of 630 ± 18 MPa at 400 °C. Overaging is delayed in Al–0.06Sc–0.06Zr by more than 100 °C as compared with the Zr-free Al–0.06Sc alloy. The Al–0.06Sc–0.06Zr alloy achieves peak microhardness after isochronal aging to 400 °C, but overages after extended annealing at this temperature (Fig. 4).
- The Al–Sc–Zr alloy exhibits creep threshold stresses of 12, 9 and 7 MPa at 300, 350 and 400 °C, respectively. This represents a small fraction of the ambient-temperature strength increment $\Delta\sigma = 138$ MPa, which is probably due to the small $Al_3(Sc_{1-x}Zr_x)$ precipitate radii, ($\langle R \rangle \sim 2$ nm). Improved creep properties are anticipated for alloys with coarsened precipitates.

Acknowledgements

This research is supported by the US Department of Energy, Basic Sciences Division, under contract DEF-G0298ER45721. We thank Prof. R. J. Tracy and Mr. C. Loehn (Virginia Tech) for performing the EPMA linescans. We are pleased to acknowledge Profs. M.E. Fine and D. Isheim (Northwestern University) and Dr. R.A. Karnesky (Sandia National Lab) for useful discussions.

References

[1] Knipling KE, Dunand DC, Seidman DN. Z Metallkd 2006;97(3):246–65.
[2] Knipling KE, Dunand DC, Seidman DN. Metall Mater Trans A 2007;38A(10):2552–63.
[3] Ryum N. Acta Metall 1969;17(3):269–78.
[4] Izumi O, Oelschlägel D. Scripta Metall 1969;3(9):619–21.
[5] Izumi O, Oelschlägel D. Z Metallkd 1969;60(11):845–51.
[6] Nes E. Acta Metall 1972;20(4):499–506.
[7] Hori S, Kitagawa T, Masutani T, Takehara A. J Japan Inst Light Metals 1977;27(3):129–37.
[8] Hori S, Kondo T, Ikeno S. J Japan Inst Light Metals 1978;28(2):79–84.
[9] Dahl W, Gruhl W, Burchard WG, Ibe G, Dumitrescu C. Z Metallkd 1977;68(3):188–94.
[10] Chaudhury ZA, Suryanarayana C. Metallography 1984;17(3):231–52.
[11] Zedalis MS, Fine ME. Metall Trans A 1986;17(12):2187–98.
[12] Knipling KE, Dunand DC, Seidman DN. Acta Mater 2008;56(1):114–27.
[13] Knipling KE, Dunand DC, Seidman DN. Acta Mater 2008;56(6):1182–95.
[14] Knipling KE, Dunand DC. Scripta Mater 2008;59(4):387–90.
[15] Ryum N. J Inst Metals 1966;94(5):191–2.
[16] Sundberg M, Sundberg R, Jacobson B. Jernkont Ann 1971;155:1–15.
[17] Rystad S, Ryum N. Aluminium 1977;53(3):193–5.
[18] Westengen H, Auran L, Reiso O. Aluminium 1981;57(12):797–803.
[19] Kashyap KT, Chandrashekar T. Bull Mater Sci 2001;24(4):345–53.
[20] Robson J, Prangnell PB. Acta Mater 2001;49(4):599–613.
[21] Robson J, Prangnell PB. Mater Sci Eng A 2003;352(1–2):240–50.
[22] Forbord B, Hallem H, Ryum N, Marthinsen K. Mater Sci Eng A 2004;387:936–9.
[23] Jia Z, Hu G, Forbord B, Solberg JK. Mater Sci Eng A 2007;444(1–):284–90.
[24] Robson J. Mater Sci Eng A 2002;338(1–2).
[25] Jia Z, Hu G, Forbord B, Solberg JK. Mater Sci Eng A 2008;483:195–8.
[26] Sigli C. In: Nie JF, Morton AJ, Muddle BC,editors, International conference on aluminum alloys (ICAA 9). Brisbane, Australia; 2004. p. 1353–8.
[27] Forbord B, Hallem H, Marthinsen K. In: Nie JF, Morton AJ, Muddle BC, editors, International conference on aluminum alloys (ICAA 9). Brisbane, Australia; 2004b. p. 1179–85.
[28] Riddle Y, Sanders T. Mater Sci Forum 2000;331–337:799–803.
[29] Costello FA, Robson JD, Prangnell PB. Mater Sci Forum 2002;396–402:757–62.
[30] Riddle Y, Hallem H, Ryum N. Mater Sci Forum 2002;396–402:563–8.
[31] Robson J. Acta Mater 2004;52(6):1409–21.
[32] Riddle Y, Sanders T. Metall Mater Trans A 2004;35A(1):341–50.
[33] Forbord B, Hallem H, Marthinsen K. In: Nie JF, Morton AJ, Muddle BC, editors. International conference on aluminum alloys (ICAA 9). Brisbane, Australia; 2004c. p. 1263–9.
[34] Clouet E, Nastar M, Barbu A, Sigli C, Martin G. Adv Eng Mater 2006;8(12):1228–31.
[35] Lieblich M, Torralba M. J Mater Sci 1991;26(16):4361–8.
[36] Lieblich M, Torralba M. J Mater Sci 1992;27(13):3474–8.
[37] Elagin V, Zakharov V, Pavlenko S, Rostova T. Phys Met Metall 1985;60(1):88–92.
[38] Davydov V, Elagin V, Zakharov V, Rostova T. Met Sci Heat Treat 1996;38(7–8):347–52.
[39] Fuller CB, Seidman DN, Dunand DC. Acta Mater 2003;51(16):4803–14.
[40] Fuller CB, Murray JL, Seidman DN. Acta Mater 2005;53(20):5401–13.
[41] Fuller CB, Seidman DN. Acta Mater 2005;53(20):5415–28.
[42] Knipling KE, Karnesky RA, Lee CP, Dunand DC, Seidman DN. Acta Mater 2010;58(15):5184–95.
[43] Xu JH, Freeman AJ. Phys Rev B 1990;41(18):12553–61.
[44] Fujikawa SI, Sugaya M, Takei H, Hirano K. J Less-Common Met 1979;63(1):87–97.
[45] Rosen M. Metall Trans A 1989;20(4):605–10.
[46] Jo HH, Fujikawa SI. Mater Sci Eng A 1993;171(1–2):151–61.
[47] Royset J, Ryum N. Mater Sci Eng A 2005;396(1–2):409–22.
[48] Clouet E, Barbu A. Acta Mater 2007;55(1):391–400.
[49] Drits MY, Dutkiewicz J, Toropova LS, Salawa J. Cryst Res Technol 1984;19(10):1325–30.

[50] Lagneborg R, Bergman B. Met Sci 1976;10:20–8.
[51] Frost HJ, Ashby MF. Deformation-mechanism maps: the plasticity and creep of metals and ceramics. New York: Pergamon Press; 1982.
[52] Murray JL. J Phase Equil 1998;19(4):380–4.
[53] Okamoto H. Phase diagrams of dilute binary alloys. Materials Park (OH): ASM International; 2002.
[54] Kerr HW, Kurz W. Int Mater Rev 1996;41(4):129–64.
[55] Murray JL, Peruzzi A, Abriata JP. J Phase Equil 1992;13(3):277–91.
[56] Kerr HW, Cisse J, Bolling GF. Acta Metall 1974;22(6):677–86.
[57] St. John DH, Hogan LM. J Mater Sci 1982;17(8):2413–8.
[58] Ohashi T, Ichikawa R. Z Metallkd 1973;64(7):517–21.
[59] Hori S, Saji S, Takehara A. J Japan Inst Light Metals 1981;31(12):793–7.
[60] Hori S, Saji S, Takehara A. In: Masumoto T, Suzuki K, editors. Proceedings of the 4th international conference on rapidly quenched metals, vol.2. Sendai: The Japan Institute of Metals; 1981b. p. 1545–8.
[61] Chalmers B. Principles of solidification. New York: John Wiley & Sons; 1964. p. 126–8.
[62] Flemings MC. Solidification processing. New York: McGraw-Hill; 1974. p. 31–2.
[63] Kurz W, Fisher DJ. Fundamentals of solidification. 4th ed. Aedermannsdorf: Trans Tech Publications; 1998. p. 15.
[64] Knipling KE, Dunand DC, Seidman DN. Microsc Microanal 2007;13(6):503–16.
[65] Kurz W, Fisher DJ. Fundamentals of solidification. 4th ed. Aedermannsdorf: Trans Tech Publications; 1998. p. 289–92.
[66] Fujikawa SI. Def Diff Forum 1997;143–147:115–20.
[67] Knipling KE. PhD thesis. Northwestern University; 2006.
[68] Clouet E, Sanchez JM, Sigli C. Phys Rev B 2002;65(9):094105.
[69] Marumo T, Fujikawa S, Hirano K. J Japan Inst Light Metals 1973;23(1):17–25.
[70] Drits MY, Ber LB, Bykov YG, Toropova LS, Anastasyeva GK. Phys Met Metall 1984;57(6):118–26.
[71] Fuller CB, Seidman DN, Dunand DC. Scripta Mater 1999;40(6):691–6.
[72] Marquis EA, Seidman DN. Acta Mater 2001;49(11):1909–19.
[73] Seidman DN, Marquis EA, Dunand DC. Acta Mater 2002;50(16):4021–35.
[74] Marquis EA, Seidman DN, Dunand DC. Acta Mater 2003;51(1):285–7.
[75] Forbord B, Lefebvre W, Danoix F, Hallem H, Marthinsen K. Scripta Mater 2004;51(4):333–7.
[76] Clouet E, Lae L, Epicier T, Lefebvre W, Nastar M, Deschamps A. Nat Mater 2006;5(6):482–8.
[77] Lefebvre W, Danoix F, Hallem H, Forbord B, Bostel A, Marthinsen K. J Alloy Compd 2009;470(1–2):107–10.
[78] Tolley A, Radmilovic V, Dahmen U. Scripta Mater 2005;52(7):621–5.
[79] Iwamura S, Miura Y. J Japan Inst Light Metals 2006;56(2):100–4.
[80] Deschamps A, Lae L, Guyot P. Acta Mater 2007;55(8):2775–83.
[81] Clouet E, Nastar M, Barbu A, Sigli C, Martin G. In: Solid–solid phase transformations in inorganic materials; 2005. p. 1–21.
[82] Royset J, Ryum N. Int Mater Rev 2005;50(1):19–44.
[83] Tabor D. Br J Appl Phys 1956;7(5):159–66.
[84] Decker RF. Metall Trans 1973;4:2495–518.
[85] Ardell AJ. Metall Trans A 1985;16(12):2131–65.
[86] Martin JW. Micromechanisms in particle hardened alloys. Cambridge: Cambridge University Press; 1980.
[87] Nembach E. Particle strengthening of metals and alloys. New York: John Wiley & Sons; 1997.
[88] Ardell A. In: Westbrook JH, Fleischer RL, editors. Intermetallic compounds: principles and practice, vol. 2. Chichester: John Wiley & Sons; 1994. p. 257–86.
[89] Martin JW. Precipitation hardening. 2nd ed. Boston (MA): Butterworth-Heinemann; 1998.
[90] Rosler J, Arzt E. Acta Metall 1988;36(4):1043–51.
[91] Arzt E. Res Mech 1991;31(4):399–453.
[92] Arzt E. In: Ochiai S, editor. Mechanical properties of metallic composites. New York: Marcel Dekker; 1994. p. 205–23.
[93] Marquis EA, Dunand DC. Scripta Mater 2002;47(8):503–8.
[94] Xiang Y, Srolovitz D. Philos Mag 2006;86(25–26):3937–57.
[95] Marquis EA, Seidman DN, Dunand DC. Acta Mater 2003;51(16):4751–60.
[96] van Dalen ME, Dunand DC, Seidman DN. Acta Mater 2005;53(15):4225–35.
[97] Karnesky RA, Seidman DN, Dunand DC. Mater Sci Forum 2006;519–521:1035–40.
[98] van Dalen ME, Seidman DN, Dunand DC. Acta Mater 2008;56(16):4369–77.